An easy and support-free synthesis of bimetallic borates for boosting the oxygen evolution reaction

Sergio García-Dalí, Javier Quílez-Bermejo, Raj Karthik, Rafael Luan Sehn Canevesi, María T. Izquierdo, Mélanie Emo, Alain Celzard, Vanessa Fierro

An easy and support-free synthesis of bimetallic borates for boosting the oxygen evolution reaction

Sergio García-Dalí[1,2,], Javier Quílez-Bermejo[1,3], Raj Karthik[1], Rafael Luan Sehn Canevesi[1], María T. Izquierdo[4], Mélanie Emo[5], Alain Celzard[1,6], Vanessa Fierro[1,*].*

[1]Université de Lorraine, Centre National de la Recherche Scientifique (CNRS), Institut Jean Lamour (IJL), F-88000, Épinal, France.

[2]Departamento de Ciencia de los Materiales e Ingeniería Metalúrgica, Universidad de Oviedo, 33004, Oviedo, Spain.

[3]Departamento de Química Inorgánica and Instituto de Materiales, Universidad de Alicante, Ap. 99, 03080, Spain.

[4]Instituto de Carboquímica (ICB-CSIQ), Miguel Luesma Castán 4, E-50018, Zaragoza, Spain.

[5]Université de Lorraine, Centre National de la Recherche Scientifique (CNRS), Institut Jean Lamour (IJL), F-54000, Nancy, France.

[6]Institut Universitaire de France (IUF).

Keywords: Oxygen evolution reaction; electrocatalysts; cobalt borates; transition metal doping; bimetallic borates.

ABSTRACT

The sluggish kinetics of the oxygen evolution reaction (OER) is one of the most limiting factors for the development of many “green” electrochemical devices. Expensive ruthenium and iridium oxide electrodes are often used as advanced electrocatalysts to overcome this limitation. However, these materials are rare in nature, which further limits the implementation of this kind of electrochemical device on a global scale. Compounds based on transition metals and boron have proven to be a promising alternative to commercial electrocatalysts due to their high catalytic properties and robust stability under working conditions. However, such compounds are often obtained through expensive synthetic routes that often involve the use of supports, which increases the cost of electrocatalysts. Here we present an easy and support-free synthesis of bimetallic borates based on the introduction of transition metals into cobalt borates. Depending on the metal, different morphologies, structural order, surface chemistry and, most importantly, electrocatalytic properties towards OER have been obtained. Among all the transition metals, nickel is the one that most improves the catalytic activity of cobalt borate for OER in an alkaline electrolyte. An overpotential of 230 mV, similar to that of commercial and state-of-the-art electrocatalysts, was obtained by using a support-free synthesis route for the preparation of this catalyst.

1. Introduction

The International Panel on Climate Change (IPCC) has warned that the world is facing the threat of dangerous global warming.[1] Hydrogen, as an energy carrier, has been proposed as a promising alternative to mitigate most of the problems of our fossil fuel-based energy economy,[2–4] since it can be obtained from water through renewable processes (solar photovoltaics, hydroelectricity, wind power, etc.) and can be used in multiple green technologies to produce energy when needed.[5,6] One of the most interesting alternatives to produce H_2 on a large scale is electrochemical water splitting (ECWS). One of the reactions involved in this process is the oxygen evolution reaction (OER), which requires electrocatalysts that perform as anodes for electrolysis.

To date, the most widely used commercial electrocatalysts for the OER are based on RuO_2 and IrO_2.[7] Despite the emergence of other materials as efficient electrocatalysts with excellent performance,[8,9] their scarcity and high cost of synthesis make their large-scale implementation extremely difficult. To solve this problem, other materials based on transition metals and non-metallic materials have emerged as active and less expensive catalysts for electrocatalytic reactions.[10–23] In particular, transition metal borates (hereinafter referred to as TMB_is, where TM is a transition metal and B_i is a borate, the subscript i indicating the inorganic nature of the boron species involved) have received much attention in recent years due to their environmental safety, low-cost and natural abundance on Earth. Cobalt borates (CoB_is), the most studied TMB_is, are believed to catalyze the hydroxylation step in the water splitting mechanism, making them very promising as electrocatalysts for OER.[24–27] In this regard, other TMB_is, such as nickel borates, have been studied as efficient electrocatalysts for OER.[28,29] However, the preparation of these materials is costly and requires tedious synthesis routes. Moreover, TMB_is used as catalysts for OER are usually prepared on conductive materials, such as Ni foam,[30,31] Ti mesh,[24] carbon cloth[26]

or self-supported graphene,[32] in order to improve their performance. These supports increase the cost and difficulty of the process, making the implementation of TMB_is as OER anodes more difficult. Subsequently, co-doped CoB_is, such as nickel-cobalt[30,32,33] or iron-cobalt borates,[31] can modify the oxidation state of Co atoms in pristine CoB_i, inducing and providing new active sites for electrocatalytic reactions, appearing as advanced catalysts for OER. However, to the best of our knowledge, no detailed analysis of the effect of different co-doped agents in CoB_is has been reported. Therefore, an easy and low-cost synthesis method of unsupported, highly catalytic co-doped CoB_is is imperative to take them to the next level of implementation and large-scale production.

Here, support-free co-doped CoB_is (M@CoB_i, where M is the transition metal co-doping agent) were systematically synthetized by a one-step method followed by heat treatment at 350 ºC. The morphology, textural properties and chemical nature of the materials were characterized by TEM, N_2 adsorption isotherms, XRD and XPS. In addition, the catalytic activity towards the OER was studied in alkaline medium. Ni@CoB_i showed outstanding catalytic properties towards OER, with an onset potential E_{OER} of 1.56 V vs. RHE and an overpotential of 230 mV (obtained at j = 10 $mA \cdot cm^{-2}$), which is a competitive value compared to similar TMB_is supported on conductive materials, and is close to the catalytic activity of the commercial ruthenium-based electrocatalyst.

2. Experimental

2.1. Synthesis of support-free bimetallic cobalt borates (M@CoB_i)

$CoCl_2 \cdot 6H_2O$ (96-97%), $Mn(NO_3)_2 \cdot 4H_2O$ (98.5%), $Zn(NO_3)_2 \cdot 6H_2O$ (98%), $Ni(NO_3)_2 \cdot 6H_2O$ (98%), $Fe(NO_3)_3 \cdot 9H_2O$ (99%) and $NaBH_4$ (98%) were supplied by Prolabo, Merck, Riedel-de

Haën, Alfa Aesar, Acros Organic and Sigma Aldrich, respectively. Nafion® (5 wt.%) perfluorinated resin solution was purchased from Sigma Aldrich.

The preparation of M@CoB_i was performed by a simple chemical reduction method combining different metals in the synthesis. 50 mL of an aqueous solution of the co-metal precursor ($Mn(NO_3)_2$, $Zn(NO_3)_2$, $Ni(NO_3)_2$ or $Fe(NO_3)_3$) at a concentration of 0.1 M were added to 50 mL of 0.3 M $CoCl_2$. Then, 15 mL of 0.3 M $NaBH_4$ were finally added. Here, $NaBH_4$ was used exclusively as the boron source, so to avoid complete reduction of the salts and obtain metal borates (B_is), the amount of $NaBH_4$ was lower than what is usually required to generate metal borides. The resulting mixture was kept under stirring for 30 min and the powder was recovered by filtration, and then washed with water and ethanol on the same filter. At this point, the non-treated metal borates are named NT-M@CoB_is. Then, the mixture was heat-treated at 350 ºC (heating rate of 1 ºC/min) for 2 h under Ar flow, yielding M@CoB_i nanoparticles. Figure 1 shows the corresponding schematic of the preparation process of the M@CoB_is.

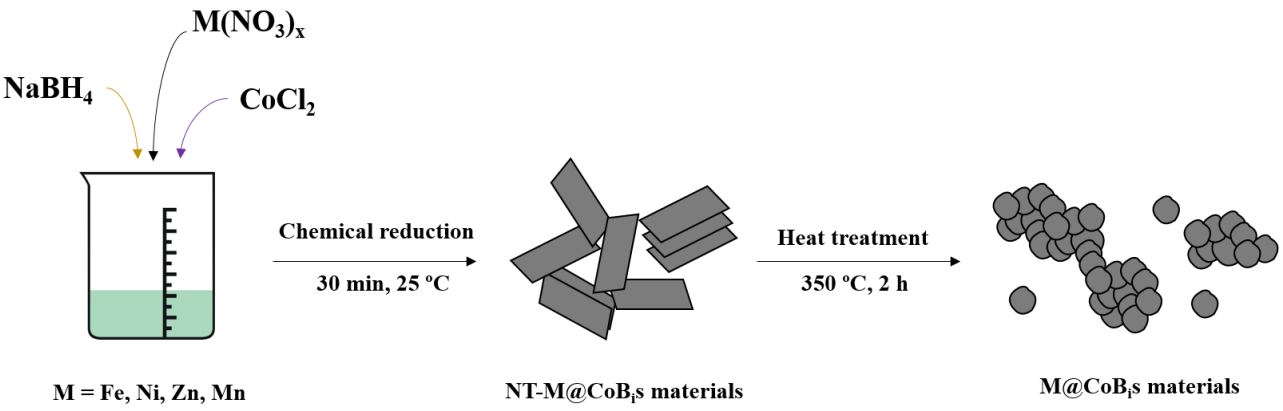

Figure 1. Schematic of the synthesis process of M@CoB_is (M = Fe, Ni, Zn and Mn), leading to more or less agglomerated nanoparticles, depending on the doping metal.

2.2. Physicochemical characterization

All prepared materials were characterized by X-ray photoelectron spectroscopy (XPS), transmission electron microscopy (TEM) and high-resolution transmission electron microscopy (HRTEM), energy-dispersive X-ray spectroscopy (EDX), X-ray diffraction (XRD) and N_2 adsorption. XPS spectra were obtained using an ESCAPlus OMICRON spectrometer equipped with a non-monochromatized Mg Kα X-ray source. Shirley-type background subtraction, peak fitting and quantification were processed using CASA software.

The textural properties of the TMB_is were obtained using non-linear density functional theory (NLDFT) applied to adsorption data obtained with nitrogen (N_2) as probe molecule. N_2 adsorption isotherms were performed at -196 ºC in a fully automated ASAP2020 manometric adsorption unit (Micromeritics, Atlanta, GA). All adsorption experiments were carried out after outgassing under high vacuum (1.3 × 10-5 mbar) and 110 ºC for at least 12 h. Total pore volume and total surface area, as well as pore size distribution (PSD), were calculated using NLDFT models in SAIEUS® software (Micromeritics, Atlanta, GA).[34,35]

The particle size distribution of heat-treated samples was determined by laser diffraction using a Mastersizer 3000 analyzer (Malvern Panalytical) after dispersion in distilled water. The crystal phases of all samples were determined using a Bruker D8 Advance A25 polycrystalline powder X-ray diffractometer. TEM and HRTEM images were acquired with a JEOL JEM – ARM 200 F Cold FEG microscope equipped with a spherical aberration (Cs) probe corrector and operating at 200 kV. The corresponding samples were prepared by dispersing the powdered material in ethanol by low-power sonication. Then, a drop of the suspension was deposited on a carbon-coated copper

TEM grid (200 mesh) and air-dried. EDX results were obtained with a JEOL spectrometer (SDD) in STEM mode.

2.3. Electrochemical measurements

The electrochemical characterization of the M@CoB_is, was carried out using a traditional three-electrode cell with a rotating ring-disk electrode (RRDE) connected to a PGSTAT302N bi-potentiostat (Metrohm). The working electrode consisted of a glassy carbon disk (0.196 cm^2) and a platinum ring as a second working electrode, the reference electrode was a reversible hydrogen electrode (RHE), and the counter electrode was a glassy carbon rod (8 mm diameter). Electrochemical measurements were performed in N_2-saturated alkaline (1 M KOH) and neutral (1M Na_2SO_4) media at room temperature, using ultrapure water as solvent. To prepare the working electrodes, the materials were suspended (4 mg mL^{-1}) in an isopropanol/water (20/80, v/v) solution containing 0.2 wt.% of Nafion®. Four aliquots of 8.42 µL of the resulting ink were then drop-cast onto the glassy carbon disk until a carbon loading of 0.68 mg·cm^{-2} was reached. To improve the wettability of the electrodes, all materials were immersed in the working solution under vacuum for a few minutes, according to a method for optimizing electrode preparation detailed elsewhere.[36] Then, each electrode was introduced into the working solution under continuous nitrogen bubbling. To stabilize the electrode, cyclic voltammetry (CV) scans from 1.00 to 0.00 V vs. RHE were recorded at a scan rate of 50 mV s^{-1} (20 cycles). Then, linear sweep voltammetry (LSV) measurements were carried out at 1600 rpm with a scan rate of 5 mV s^{-1} from 0.80 V to 1.80 V vs RHE. Under these conditions, the onset potential (E_{OER}), as well as the overpotential (i.e., the extra potential needed to oxidize water to oxygen gas compared to the theoretical redox potential (1.23 V)) were obtained at 10 mA·cm^{-2} and used as standard values to compare the catalytic activity of

different electrocatalysts. The currents were always normalized by the geometric area of the disk (0.196 cm^2). The Faradaic efficiency was determined by the following equation:[37]

$$(n_{Disk}/n_{Ring})\ i_{Ring}/(N\ i_{Disk}) \quad (1)$$

where n_{Disk} and n_{Ring} are the number of electrons transferred in the OER at the disk and ring electrode, respectively. It was assumed that 4 electrons were transferred in both cases, as it is well known that Pt reduces O_2 molecules through the 4-electron pathway. N is the ring collection efficiency (0.27 in this case) and i_{Disk} and i_{Ring} are the current densities recorded in the disk and ring electrodes, respectively. The platinum ring was fixed at a constant potential of 0.3 V vs RHE.

3. Results and discussion

Figure 2 shows TEM images of the materials obtained before heat treatment (NT-M@CoB_is) schematized by the second step in Fig. 1. A 2D lamellar conformation was obtained for all materials. Selected area electron diffraction (SAED) patterns (insets in Figure 2) show broad rings indicating that the materials are partially crystallized.

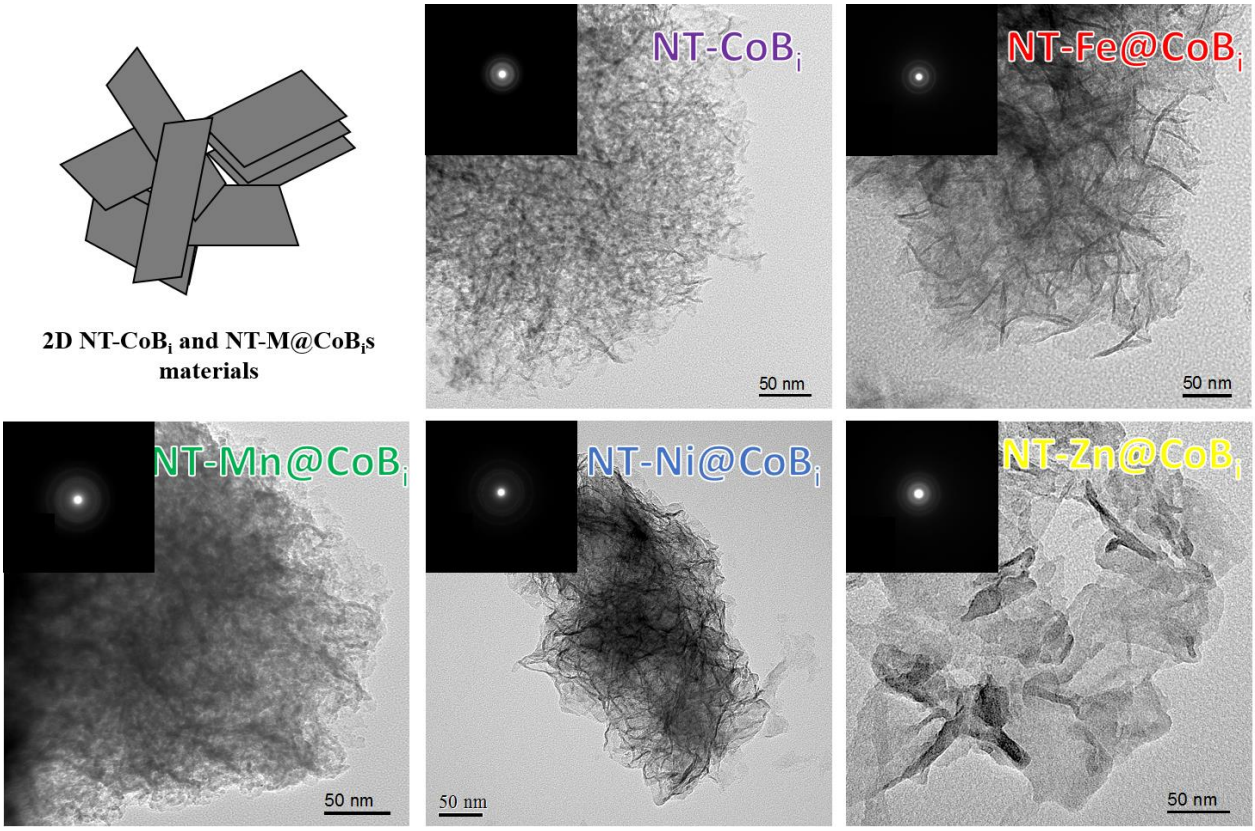

Figure 2. TEM images and SAED patterns (insets) of NT-CoB_i, NT-Fe@CoB_i, NT-Mn@CoB_i, NT-Ni@CoB_i and NT-Zn@CoB_i.

After the heat treatment, the surface chemistry of the materials was characterized by XPS and the atomic composition of the material surface is summarized in Table 1. As can be observed, the abundance of Co is highly dependent on the nature of the co-metal, although the same concentration was used in all cases. The Co content in the CoB_i material is about 16 at.%, while the Co contribution is reduced with the addition of the co-metals. This reflects the fact that part of the co-metal replaces the initial Co cations when Fe, Co, Zn or Mn are introduced in the synthesis. In general, the higher the Co content of the M@CoB_i materials, the lower the content of the co-agent. For instance, the incorporation of Mn into CoB_i leads to a Co content of 15 at.% and only 2.9 % Mn in the Mn@CoB_i material. Conversely, the lowest Co content was determined in the Zn@CoB_i material, with 7.4 at.% Co and 7.6 at.% Zn. The maximum total metal content was

reached in Fe@CoB_i, with 11.4 at.% Fe and 11.2 at.% Co. Fe@CoB_i and Zn@CoB_i have approximately the same co-metal /cobalt (M/Co ratio), around 1, while in Ni@CoB_i and Mn@CoB_i, the M/Co ratio is 0.5 and 0.2, respectively. The variation of the B content also strongly depends on the co-metal, Zn@CoB_i being the material with the highest surface B content (31 at.%) and Fe@CoB_i the one with the lowest B content, with only 14.7 at.%. In addition, all samples exhibit high O content, which is in agreement with the formation of metal borates, as well as some metal oxides on the surface of the materials, as it is known that some of the metal content in CoB_i is in the form of surface cobalt oxides.[38]

Table 1. Atomic percentage of doping metal (M), cobalt (Co), oxygen (O) and boron (B) obtained by XPS, and metal/cobalt (M/Co) and Co^{3+}/Co^{2+} atomic ratios.

Sample	Co [at%]	Co^{3+}/Co^{2+} atomic ratio	Co-metal [at%]	M/Co atomic ratio	O [at%]	B [at%]
CoB_i	16.2	1.65	-	-	56.5	27.3
Fe@CoB_i	11.2	3.28	11.4	1.02	62.7	14.7
Mn@CoB_i	17.9	3.11	2.9	0.16	56.0	23.1
Ni@CoB_i	13.3	4.06	6.0	0.45	56.9	23.8
Zn@CoB_i	7.4	2.09	7.6	1.02	53.9	31.0

To evaluate the oxidation states of the element Co, the Co $2p_{3/2}$ spectra (Fig. 3) of all materials were analyzed. Two main peaks were located at 780.7 ± 0.2 eV and 782.7 ± 0.2 eV, which are

related to the presence of Co^{3+} and Co^{2+}, respectively.[39] In addition, the satellite peak was located at 785-787 eV. However, the ratio of Co^{3+} to Co^{2+} is a valuable indicator for evaluating the oxidation state of the cobalt species in the M@CoB_i materials. The Co^{3+}/Co^{2+} ratio increases in all samples compared to pristine CoB_i (see Table 1), with Ni being the metal that induces the greatest Co^{3+} conversion. This means that after the addition of the co-metals, the Co species that remain in the material are those with the highest oxidation states, while Co^{2+} appears to be the metal species that is mostly replaced by the co-metal atoms. Furthermore, the Co^{3+}/Co^{2+} ratio does not depend on the co-metal level but on the nature of the co-metal. This is particularly noticeable when comparing Ni as co-metal, in which a Co^{3+}/Co^{2+} ratio of 4.06 was the highest observed, with a M/Co ratio of 0.45, and Zn, in which the Co^{3+}/Co^{2+} ratio was the lowest (2.09) with the highest M/Co ratio (1.02).

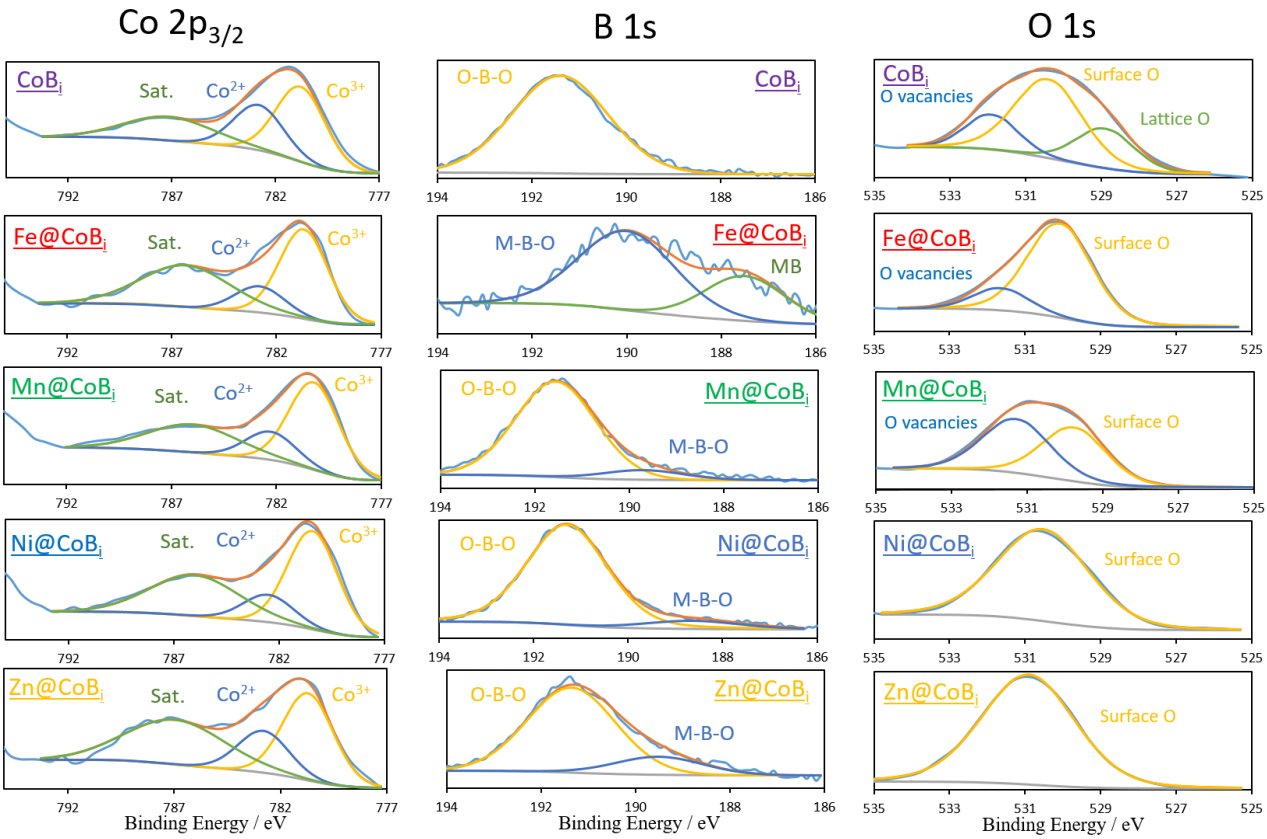

Figure 3. XPS spectra of Co $2p_{3/2}$ (left column), B 1s (middle column) and O 1s (right column) of each material synthesized.

The B 1s spectra (Figure 3) of all materials indicate the presence of two oxidized states of boron, at 191.4 ± 0.2 eV and 189.5 ± 0.2 eV, related to the presence of O-B-O and M-B-O[40] species, respectively. In general, all materials show mainly the O-B-O contribution, but only Fe@CoB_i, Zn@CoB_i and Mn@CoB_i show the presence of an M-B-O peak. At the same time, Fe@CoB_i is the only sample in which a third peak is observed, at 187.5 ± 0.2 eV. This peak could be related to the presence of metal borides (CoB).[38] However, the Co $2p_{3/2}$ spectra did not show the contribution of CoB, and FeB was not detected either in the Fe $2p_{3/2}$ spectra, as it is shown in Figure S1. Based on these results, it is suggested the formation boron particles on the surface of Fe@CoB_i.[41]

The O 1s spectra (Figure 3) indicate the presence of three different species in the pristine CoB_i material. The first contribution appears at 529.1 ± 0.2 eV, which was attributed to lattice O, corroborating the formation of cobalt oxide on the surface. The main peak at 530.6 ± 0.2 eV is related to -OH groups on the surface of the material, and the third peak at 532.1 ± 0.2 eV is associated with oxygen vacancies.[42] Interestingly, after the incorporation of the co-metal, the peak related to lattice O disappears completely, leading to -OH groups in the Ni@CoB_i and Zn@CoB_i samples and both -OH groups and O vacancies in the Fe@CoB_i and Mn@CoB_i materials, with the formation of O vacancies being especially marked with the incorporation of a small amount of Mn. In addition, a slight shift in the binding energies of the peaks related to -OH groups and O vacancies is observed. This is due to the new interaction of the -OH groups with the additional metal introduced, which creates a different electron density in the surface chemistry of the M@CoB_i materials. Furthermore, the individual spectrum of each co-doped metal was also identified, confirming the successful formation of M@CoB_is. Figure S1 shows that all co-metals exhibit positively charged oxidation states, with Mn@CoB_i being exclusively the material in which the doping metal is also in the metallic state. All doping metals were found in different oxidation states (Fig. S1).[43–45]

To determine the crystallization degree and identify the phases present in each sample, XRD was used (Figure 4). The pristine CoB_i shows a poorly crystallized structure with broad peaks associated with CoO, but also has a well-defined peak at ~44.5º, which corresponds to crystallized domains of CoB_i.[46] The introduction of a second metal species does not produce a complete crystallization of the material. Nevertheless, it is worth noting that the addition of the co-metals in CoB_i induces significant changes in the crystallization degree of the original structure, leading to a different structural order of the metal borates. While a more ordered structure is observed in

Fe@CoB_i and Zn@CoB_i, Mn@CoB_i and Ni@CoB_i show a more disordered structure similar to that of amorphous CoB_i. This means that the introduction of Fe and Zn during the synthesis of M@CoB_i induces significant changes in the structural order of the materials, since a higher crystallization degree is clearly observed. Moreover, the metallic co-doping metal agents appear to have a significant role in the formation of crystalline phases, as indicated by the occurrence of new peaks in the XRD profiles. This is likely related to the high amount of co-doping metal incorporated into the CoB_i structure. The use of Fe during the synthesis also leads to the predominance of peaks related to iron oxide nanoparticles,[47] while the contribution of CoO and CoB_i is not observed in the XRD profile. The same behavior is observed in the Zn@CoB_i sample. The CoO and CoB_i bands are not observed in the XRD profile, but only peaks of zinc borate are visible.[48] Therefore, the synthesis strategy not only leads to the formation of CoB_is, but also to the formation of co-doped metal borates depending on the nature of the metallic co-doping agent.

Interestingly, according to XPS, the samples in which the most significant morphological changes are observed are those in which the concentration of the metal doping agent is the highest. Fe@CoB_i and Zn@CoB_i are indeed the samples with the highest co-metal content, which favors different chemical features than those observed in the pristine material. On the other hand, the Mn@CoB_i sample, which has the lowest co-metal level (Mn content = 2.9 at.%, see Table 1), shows a similar disordered-type XRD profile as the pristine CoB_i, since the CoB_i and CoO phases still predominate. Nevertheless, it is interesting to note that the incorporation of a small amount of Mn induces a slight crystallization degree in the CoB_i structure without the formation of manganese oxides or borates.

The Ni@CoB_i sample shows an unusual behavior compared to other co-metallic materials since, despite its high Ni content, Ni@CoB_i still exhibits the XRD profile of a poorly crystallized material

similar to pristine CoB_i, besides the presence of NiO[49] and NiB_i[32] phases (Figure 4). This means that the introduction of large amounts of Ni does not significantly disturb the crystallization degree of the pristine CoB_i, contrary to other co-metal such as Fe or Zn, which may be interesting for maintaining the excellent chemical properties of CoB_i with small variations in the oxidation states of the materials.

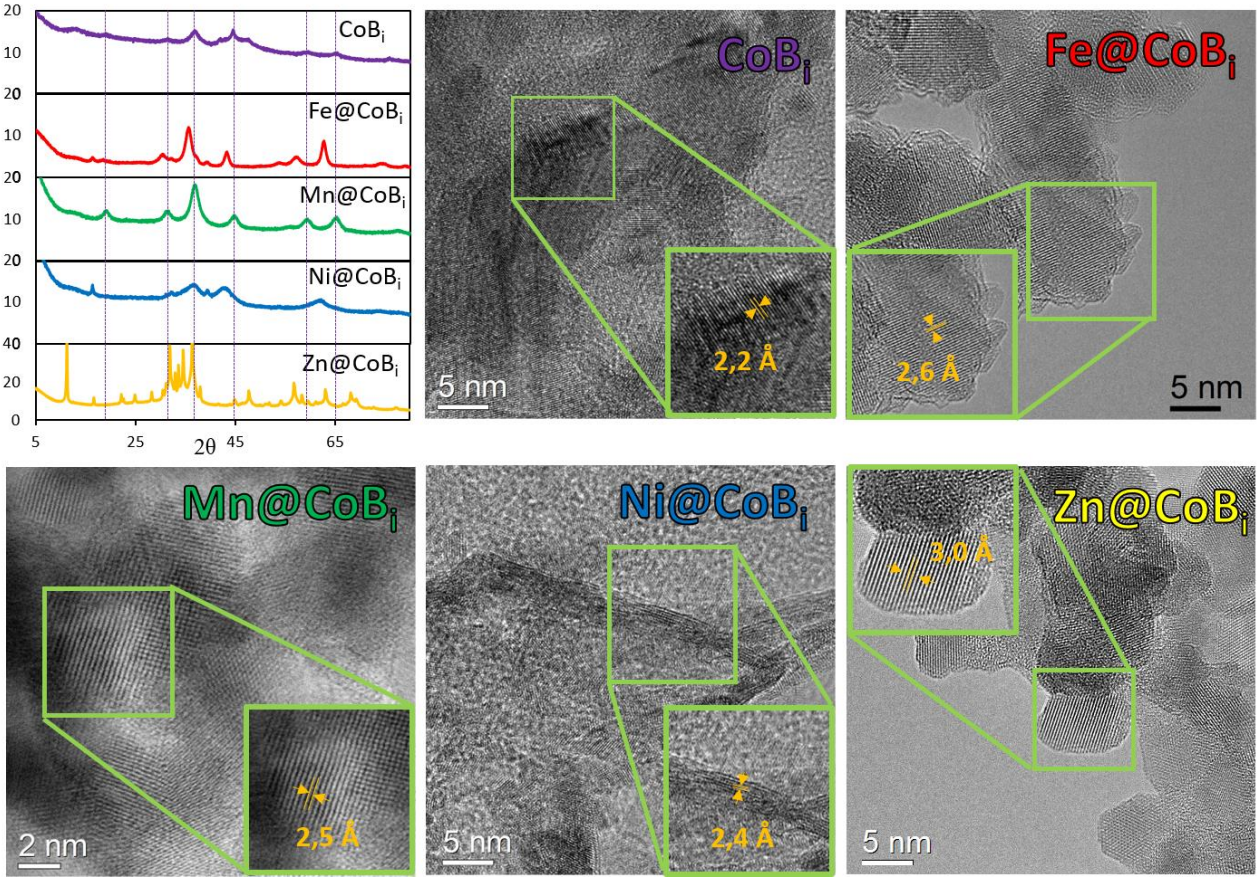

Figure 4. XRD patterns and HRTEM images of CoB_i, $Fe@CoB_i$, $Mn@CoB_i$, $Ni@CoB_i$ and $Zn@CoB_i$ with the corresponding determination of the inter-planar spacing (insets).

The SAED patterns (insets in Figure S2-S6) show intense rings and dots indicating that the materials are more crystallized after heat treatment. TEM observations (Figures S2-S6) reveal the presence of nanoparticles with spherical morphology in CoB_i. However, the introduction of co-metals produces changes in the morphology of the materials as follows. $Fe@CoB_i$ and $Zn@CoB_i$ samples, which exhibit the highest crystal order according to XRD, clearly show less aggregated,

rod-shaped or nanosphere-shaped nanoparticles, respectively. On the other hand, Mn@CoB_i and Ni@CoB_i samples, which exhibit the lowest crystal order accordingly to XRD, show an extremely high degree of particle agglomeration, making it impossible to identify the morphology of the synthesized nanoparticles. The introduction and presence of co-metals in the synthesized samples was further confirmed by EDX results (Figure S7), in which all co-metals were detected. Moreover, some traces of chlorides from the metal reagents were also detected, as they were not totally removed during the heat treatment step. In addition, HRTEM images were acquired to measure the inter-planar spacing of the as-prepared materials. Figure 4 shows that the incorporation of the co-doping metals induces an increase in the inter-planar spacing of the pristine CoB_i (2.2 Å). The higher inter-planar spacing when using co-doping metal agents could be attributed to the presence of newly formed crystalline phases, such as those corresponding to Ni, Fe and Zn borates.[32,50,51] Interestingly, the highest inter-planar spacing is reached in Zn@CoB_i (3.0 Å), which is likely related to the lower Co content of this material (see Table 1). Thus, this high inter-planar spacing might be related to Zn-related crystalline phases, in agreement with the XRD experiments. The inter-planar spacing of the M@CoB_is seems to be strongly related to the chemical composition after co-doping.[52]

Table 2. BET area (A_{BET}), total pore volume (V_T) and micropore volume (V_{micro}) obtained from N_2 adsorption isotherms at -196 °C.

Samples	A_{BET} / m^2 g^{-1}	V_T / cm^2 g^{-1}	V_{micro} / %
CoB_i	70	0.01	5.3
Fe@CoB_i	32	0.01	0.5
Mn@CoB_i	231	0.04	1.4
Ni@CoB_i	282	0.04	2.3
Zn@CoB_i	112	0.03	1.9

The particle size distribution of the heat-treated materials was determined by laser diffraction of the materials dispersed in water, and the results are shown in Figure S8. CoB_i exhibits a broad and bimodal particle size distribution with peaks centered at ~8 and ~45 µm. The introduction of other metals in CoB_i induced a decrease in particle size, Fe@CoB_i being the material with the smallest particle size (~8 µm), as expected from the non-agglomerated particles observed by TEM. The Zn@CoB_i sample shows a broad particle size distribution, even broader than CoB_i, but with the main particle size around 20 µm. In good agreement with the TEM images, Ni@CoB_i and Mn@CoB_i exhibit an almost identical particle size distribution with a maximum of about 13 µm.

N_2 adsorption isotherms (Figure S9) were used to study the textural properties and BET area (A_{BET}) of CoB_i-based materials. The A_{BET} results are presented in Table 2. The A_{BET} of pristine CoB_i is 70 $m^2 \cdot g^{-1}$ and the addition of the metal doping agents leads to significant differences in A_{BET}. The introduction of Fe into the synthesis of CoB_i led to the highest metal content with a highly

crystallized structure, thus producing a decrease in the A_{BET} of the resulting material (32 $m^2 \cdot g^{-1}$). In contrast, the introduction of Ni into the CoB_i structure led to a disordered structure similar to pristine CoB_i according to XRD, but with a significantly higher A_{BET} (282 $m^2 \cdot g^{-1}$). Intermediate A_{BET} values were determined for Mn@CoB_i and Zn@CoB_i. Total volume and micropore volume are also gathered in Table 2. However, no significant differences were detected in these parameters, showing similar trends to that obtained in A_{BET}. It is worth noting that, according to the N_2 adsorption isotherms, the samples are mainly mesoporous materials, with a small contribution of micropores.

The electrocatalytic activity towards the OER of all materials was evaluated in a 1.0 M KOH solution saturated with N_2. Cyclic voltammetry (CV) was performed, and shown in Figure S10, as an initial study to determine the formation of the double-layer and to investigate the effect of materials properties, such as electrical conductivity, A_{BET} and hydrophilicity, on its performance. Despite very different A_{BET} values, no significant changes were detected in the double layer formation in CoB_i, Zn@CoB_i, Mn@CoB_i and Zn@CoB_i, and no redox peaks were observed either, suggesting that no changes in electrical conductivity or hydrophilicity, which would promote double-layer formation, have been produced from CoB_i to Zn@CoB_i, Mn@CoB_i and Zn@CoB_i. Interestingly, only Fe@CoB_i exhibits a broad peak, close to 0 V, related to the reduction of some species exposed at the surface. Fe@CoB_i is the sample with the highest co-metal content on the surface, according to XPS, and it is reasonable to associate this broad peak with the reduction of Fe species on the surface.

Figure 5a shows the linear sweep voltammetry (LSV) curves for all materials in the OER, performed with a rotating ring-disk electrode (RRDE) at 1600 rpm and 5 $mV \cdot s^{-1}$. CoB_i exhibits an E_{OER} of 1.63 V vs RHE, which is similar to other cobalt borates studied in the literature (Figure

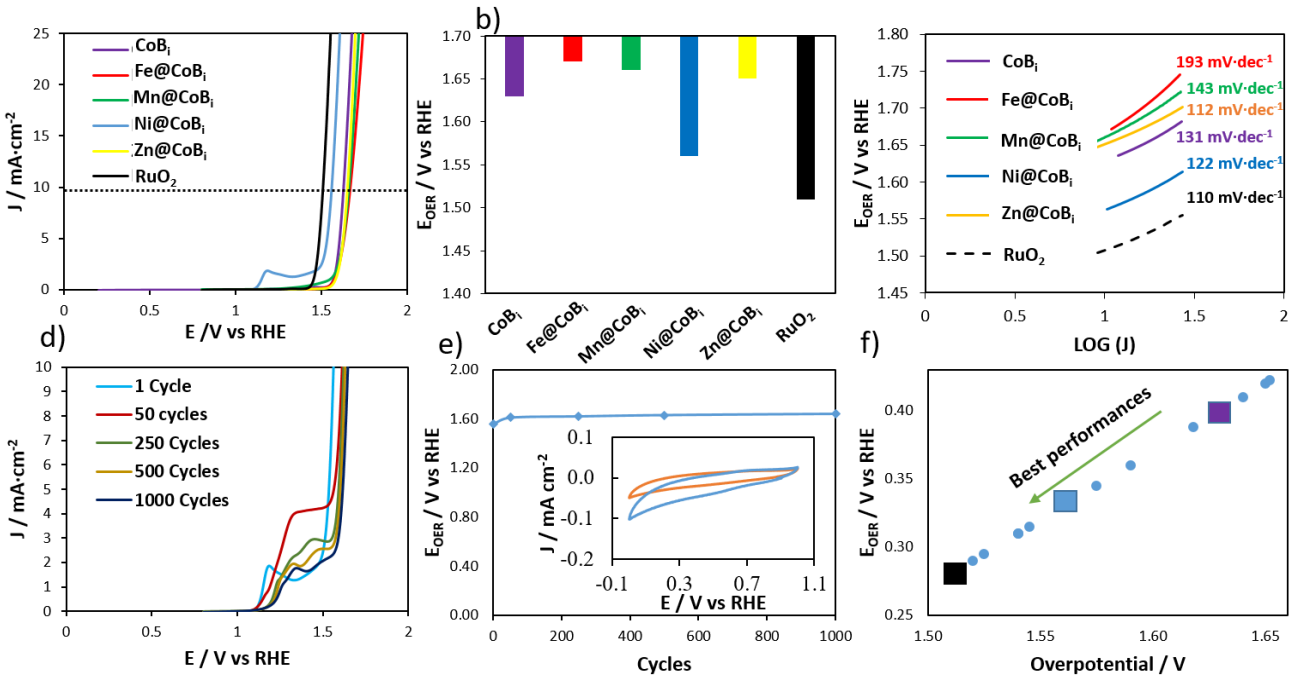

Figure 5. (a) LSV curves; (b) schematic representation of the E_{OER} potential; and (c) Tafel slopes of all materials for OER in 1 M KOH, including commercial RuO_2. (d) LSV curves of Ni@CoB_i catalyst during 1000 cycles for OER in 1 M KOH; and (e) schematic representation of its E_{OER} potential, as well as the CVs before (orange curve) and after (blue curve) the OER. (f) Graphical comparison of 3 of the materials prepared (large squares) with other similar materials found in the literature (small circles).

5f). The introduction of different co-metals strongly influences the catalytic activity of the OER. Zn@CoB_i, Mn@CoB_i and Fe@CoB_i show a decrease in catalytic activity, which is reflected in an increase of the E_{OER} up to 1.65, 1.66 and 1.67 V vs RHE, respectively (Figure 5b), demonstrating that the introduction of these metals is detrimental to the catalytic performance towards the OER of CoB_i. However, the introduction of Ni into CoB_i significantly improves the electrocatalytic activity compared to pure CoB_i, reaching an E_{OER} of 1.56 V vs RHE. This high catalytic activity is close to that of the state-of-the-art M@CoB_is, and similar to that of commercial RuO_2-based electrocatalysts (E_{OER} = 1.52 V). For comparison, NT-M@CoB_is samples were also studied for OER, as shown in Figure S11. In all cases, heat treatment produces an increase in electrochemical activity, when NT-M@CoB_is are compared with M@CoB_is. Heat treatment at 350 ºC induces

chemical changes in the structural order of the materials that allow the introduction of the metal doping agent into the chemical structure of the pristine CoB_i. As shown by XRD, different phases are obtained depending on the metal co-doping agent during heat treatment, which has consequence on the resulting electrocatalytic activity towards the OER. Due to the high industrial interest in water electrolysis at neutral pH, OER was also tested in neutral solution, using N_2-saturated 1M Na_2SO_4 electrolyte, as shown in Figure S12. Under neutral pH, the M@CoB_is exhibit poor performance, suggesting that the presence of OH^- ions in the solution plays a key role in the high electrocatalytic activity achieved by Ni@CoB_i in alkaline medium. This is related to different OER mechanisms and kinetics depending on the pH. At neutral pH, adsorption of water molecules is the first step in OER, while adsorption of OH^- is the first step in alkaline media.[53]

The Tafel slopes (Figure 5c) show that Fe@CoB_i and Mn@CoB_i suggest sluggish kinetics compared to CoB_i. However, the Tafel slopes of the materials obtained after the addition of Ni and Zn (Ni@CoB_i and Zn@CoB_i) are lower than those of CoB_i; this indicates an improvement in kinetics towards the OER that approaches the performance of RuO_2. Interestingly, the Zn@CoB_i material, which shows poor catalytic activity, achieves a lower Tafel slope (112 $mV \cdot dec^{-1}$) than that of Ni@CoB_i and is comparable to that of RuO_2 (110 $mV \cdot dec^{-1}$).

Long-term chronoamperometric analysis was performed to evaluate the stability of the most catalytic sample for the OER. Figure 5d shows the LSV curves after 50, 250, 500 and 1000 cycles for the Ni@CoB_i material, which shows high stability even after 1000 cycles, with a slight decrease in E_{OER} from 1.56 to 1.64 V vs RHE. This decrease is mainly produced during the first cycles, in which the catalytic activity varies from 1.56 to 1.61 V after the first 50 cycles. From the 50th cycle to the 1000th cycle, the catalytic activity remains almost constant (Figure 5e). The CV profile of Ni@CoB_i after the 1000 cycles of the stability test were performed and compared with that of the

pristine Ni@CoB_i, in order to observe possible chemical changes under the OER working conditions. Similar CV profiles before and after the stability test were obtained, demonstrating the high stability of the material. Moreover, as shown in Figure 5e, slight differences in the CV profile can be obtained after 1000 cycles (blue curve). The CV profile after 1000 cycles exhibits a higher cathodic current density at negative potential (0.0 – 0.3 V vs. RHE), indicating small chemical changes in the material. The oxidative conditions in the OER experiments generate a slight modification of the surface chemistry of Ni@CoB_i. This effect is probably produced by the intercalation of the electrolyte into the material, which generates a higher exposed area and increases the gravimetric capacitance.[54] In addition, the Faradaic efficiency of all materials was studied in Figure S13. As can be observed, the use of a co-doping metal produces a striking increase in the maximum Faradaic efficiency, from 10% in the case of the pristine CoB_i to 85, 92 and 98 % in the case of Mn@CoB_i, Ni@CoB_i and Zn@CoB_i, respectively, reaching 100 % in the Fe@CoB_i sample. In all cases, the Faradaic efficiency decreases at high potential values due to the experimental setup as the formation of observable O_2 bubbles on the catalyst surface prevents the transfer of O_2 from the disk to the Pt ring and, therefore, this leads to the increase of i_{Ring}.[37]

A comparison of the electrocatalytic activity of M@CoB_i for the OER with the most promising MB_is from the recent literature is presented in Table S1 and Figure 5f, demonstrating the significance of the effects produced by the introduction of Ni into CoB_i. Figure 5f shows that better OER catalytic activity than those obtained in this work can only be achieved by using CoB_is with conductive substrates such as Ni foam,[31] carbon cloth (CC), [33] reduced graphene oxide (RGO)[32] and graphene (G),[55] which significantly increase the cost and production time of these catalysts. Another strategy to achieve this state-of-the-art-like performance is obtained by doping CoB_is with Ru atoms.[56] However, Ru is an expensive metal that does not overcome the problems of current

commercial electrocatalysts, making large-scale commercialization of these catalysts infeasible. In contrast, the present Ni@CoB_i exhibits state-of-the-art OER performance through the proposed synthesis method from inexpensive reagents, which significantly reduces the cost of the catalysts. Therefore, this Ni@CoB_i material is positioned among the most promising CoB_i-based electrocatalysts in the literature due to its high catalytic activity, easy synthesis and low-cost production.

These results also highlight the relevant effect of the co-metal, which strongly affects the electronic, structural and chemical properties of the pristine CoB_i. This has a negative or positive impact on the catalytic activity towards the OER, depending on the nature of the metal and the resulting structural and chemical changes. The introduction of Zn, Fe or Mn results in a decrease in the OER catalytic activity compared to the pristine CoB_i, probably due to the chemical and structural changes induced by these co-doping metals. On the other hand, Ni@CoB_i shows better OER catalytic performance compared to the CoB_i. Density Functional Theory (DFT) calculations proved that the presence of Ni in the CoB_i structure promotes the stabilization of the O· and ·OOH reaction intermediates, decreasing the free energy of the rate-determining step.[57] This, together with its disordered structure, high A_{BET}, high Co^{3+}/Co^{2+} ratio, and high Ni content, might explain the enhanced OER activity of the Ni@CoB_i material.

4. Conclusions

Support-free bimetallic catalysts based on cobalt borates (M@CoB_is), using Fe, Ni, Zn or Mn (M) as co-metal, were successfully synthesized by an easy one-step chemical reduction followed by heat treatment at 350 ºC. All the M@CoB_is, exhibited different crystal phases, agglomeration degree and A_{BET} values compared to pristine CoB_i and presented diverse behavior when tested as

electrocatalysts for OER. Interestingly, Ni@CoB_i showed the highest electrocatalytic activity for OER, with an E_{OER} of 1.56 V vs RHE, similar to commercial RuO_2.

The easy and inexpensive synthesis of support-free M@CoB_is thus appears to be a simple and promising alternative to other electrocatalysts, which often require conductive supports, expensive synthesis routes or precious metals to achieve competitive OER performance. Moreover, the wide variety of chemical and textural properties obtained from the different co-metals opens a wide field of exploration using multi-metal agents to optimize further the properties of support-free M@CoB_is, not only for electrocatalysis but also for a broad range of applications.

Author Contributions

Sergio García-Dalí: conceptualization, investigation, data curation, writing–original draft. Javier Quílez-Bermejo: conceptualization, investigation, data curation, writing–original draft. Raj Karthik : conceptualization, investigation. Rafael Canevesi: investigation, data curation. María T. Izquierdo: investigation, review & editing. Mélanie Emo: investigation, review & editing. Alain Celzard: supervision, writing – review & editing. Vanessa Fierro: conceptualization, supervision, validation, writing – review & editing, funding acquisition.

Supporting Information

Additional experimental details and results including data and figures related to XPS, HRTEM, EDX, particle size distribution, adsorption isotherms, CV curves under alkaline conditions, LSV curves under alkaline and neutral conditions and Faradaic efficiency of the different doped and non-doped cobalt borates, and comparison of their main OER electrocatalytic performance with those of other materials from the literature.

Acknowledgement

This study was partly supported by the French PIA project “Lorraine Université d’Excellence”, reference ANR-15-IDEX-04-LUE and the TALiSMAN project funded by ERDF (2019-000214). SGD thanks the Ministerio de Universidades, the European Union and the University of Oviedo for the financial support (MU-21-UP2021-030 30267158). JQB thanks the Ministerio de Universidades, the European Union and the University of Alicante for the financial support (MARSALAS21-21).

REFERENCES

(1) Masson-Delmotte, V.; Zhai, P.; Pörtner, H. .; Roberts, D.; Skea, J.; Shukla, P. R.; Pirani, A.; Moufouma-Okia, W.; Péan, C.; Pidcock, R.; Connors, S.; Matthews, J. B. R.; Chen, Y.; Zhou, X.; Gomis, M. I.; Lonnoy, E.; Maycock, T.; Tignor, M.; Waterfield, T. Summary for Polimarkers. *IPCC* **2018**, 15–39.

(2) Turner, J. A. Sustainable Hydrogen Production. *Science.* **2004**, *305* (5686). https://doi.org/10.1126/science.1103197.

(3) Chung, D. Y.; Jun, S. W.; Yoon, G.; Kim, H.; Yoo, J. M.; Lee, K. S.; Kim, T.; Shin, H.; Sinha, A. K.; Kwon, S. G.; Kang, K.; Hyeon, T.; Sung, Y. E. Large-Scale Synthesis of Carbon-Shell-Coated FeP Nanoparticles for Robust Hydrogen Evolution Reaction Electrocatalyst. *J. Am. Chem. Soc.* **2017**, *139* (19), 6669–6674. https://doi.org/10.1021/jacs.7b01530.

(4) Cipriani, G.; Di, V.; Genduso, F.; La, D. ScienceDirect Perspective on Hydrogen Energy Carrier and Its Automotive Applications. *Int. J. Hydrogen Energy* **2014**, *39* (16), 8482–8494. https://doi.org/10.1016/j.ijhydene.2014.03.174.

(5) Shinagawa, T.; Takanabe, K. Towards Versatile and Sustainable Hydrogen Production through Electrocatalytic Water Splitting: Electrolyte Engineering. *ChemSusChem* **2017**, *10* (7), 1318–1336. https://doi.org/10.1002/cssc.201601583.

(6) Jiao, Y.; Zheng, Y.; Jaroniec, M.; Qiao, S. Z. Design of Electrocatalysts for Oxygen- and Hydrogen-Involving Energy Conversion Reactions. *Chem. Soc. Rev.* **2015**, *44* (8), 2060–2086. https://doi.org/10.1039/c4cs00470a.

(7) Lee, Y.; Suntivich, J.; May, K. J.; Perry, E. E.; Shao-Horn, Y. Synthesis and Activities of Rutile IrO2 and RuO2 Nanoparticles for Oxygen Evolution in Acid and Alkaline Solutions.

J. Phys. Chem. Lett. **2012**, *3* (3), 399–404. https://doi.org/10.1021/jz2016507.

(8) Huang, W.; Li, J.; Liao, X.; Lu, R.; Ling, C.; Liu, X.; Meng, J.; Qu, L.; Lin, M.; Hong, X.; Zhou, X.; Liu, S.; Zhao, Y.; Zhou, L.; Mai, L. Ligand Modulation of Active Sites to Promote Electrocatalytic Oxygen Evolution. *Adv. Mater.* **2022**, *34* (18), 1–8. https://doi.org/10.1002/adma.202200270.

(9) Li, J.; Huang, W.; Wang, M.; Xi, S.; Meng, J.; Zhao, K.; Jin, J.; Xu, W.; Wang, Z.; Liu, X.; Chen, Q.; Xu, L.; Liao, X.; Jiang, Y.; Owusu, K. A.; Jiang, B.; Chen, C.; Fan, D.; Zhou, L.; Mai, L. Low-Crystalline Bimetallic Metal-Organic Framework Electrocatalysts with Rich Active Sites for Oxygen Evolution. *ACS Energy Lett.* **2019**, *4* (1), 285–292. https://doi.org/10.1021/acsenergylett.8b02345.

(10) Xu, Y.; Ming, H. Electrocatalysis for the Oxygen Evolution Reaction: Recent Development and Future Perspectives. *Chem. Soc. Rev.* **2017**, *46* (2), 303–562. https://doi.org/10.1039/c6cs00328a.

(11) Zhu, Y. P.; Guo, C.; Zheng, Y.; Qiao, S. Surface and Interface Engineering of Noble-Metal-Free Electrocatalysts for Efficient Energy Conversion Processes. *Acc. Chem. Res.* **2017**, *50* (4), 915–923. https://doi.org/10.1021/acs.accounts.6b00635.

(12) Zhu, W.; Zhang, R.; Qu, F.; Asiri, A. M.; Sun, X. Design and Application of Foams for Electrocatalysis. *ChemCatChem Rev.* **2017**, 9, 1721–1743. https://doi.org/10.1002/cctc.201601607.

(13) Yan, Y.; Xia, Y.; Wang, X. A Review on Noble-Metal-Free Bifunctional Heterogeneous Catalysts for Overall Electrochemical Water Splitting. *J. Mater. Chem. A* **2016**, 45, 17587–17603. https://doi.org/10.1039/c6ta08075h.

(14) Eftekhari, A. Electrocatalysts for Hydrogen Evolution Reaction. *Int. J. Hydrogen Energy*

2017, *42* (16), 11053–11077. https://doi.org/10.1016/j.ijhydene.2017.02.125.

(15) Xu, Y.; Kraft, M.; Xu, R. Metal-Free Carbonaceous Electrocatalysts and Photocatalysts for Water Splitting. *Chem. Soc. Rev.* **2016**, 45, 3039–3052. https://doi.org/10.1039/c5cs00729a.

(16) Anantharaj, S.; Ede, S. R.; Sakthikumar, K.; Karthick, K.; Mishra, S.; Kundu, S. Recent Trends and Perspectives in Electrochemical Water Splitting with an Emphasis on Sulfide, Selenide, and Phosphide Catalysts of Fe, Co, and Ni: A Review. *ACS Catal.* **2016**, *6* (12), 8069–8097. https://doi.org/10.1021/acscatal.6b02479.

(17) Jamesh, M. I. Recent Progress on Earth Abundant Hydrogen Evolution Reaction and Oxygen Evolution Reaction Bifunctional Electrocatalyst for Overall Water Splitting in Alkaline Media. *J. Power Sources* **2016**, *333*, 213–236. https://doi.org/10.1016/j.jpowsour.2016.09.161.

(18) Shi, S. Y.; Zhang, B. Recent Advances in Transition Metal Phosphide Nanomaterials: Synthesis and Applications in Hydrogen Evolution Reaction. *Chem. Soc. Rev.* **2016**, *45*, 1529. https://doi.org/10.1039/c5cs00434a.

(19) Quílez-Bermejo, J.; Morallón, E.; Cazorla-Amorós, D. Metal-Free Heteroatom-Doped Carbon-Based Catalysts for ORR. A Critical Assessment about the Role of Heteroatoms. *Carbon.* **2020**, *165*, 434–454. https://doi.org/10.1016/j.carbon.2020.04.068.

(20) Zhang, T.; Song, F.; Qian, Y.; Gao, H.; Shaw, J.; Rao, Y. Elemental Engineering of High-Charge-Density Boron in Nickel as Multifunctional Electrocatalysts for Hydrogen Oxidation and Water Splitting. *ACS Appl. Energy Mater.* **2021**, *4* (6), 5434–5442. https://doi.org/10.1021/acsaem.0c03179.

(21) Im, S. W.; Ahn, H.; Park, E. S.; Nam, K. T.; Lim, S. Y. Electrochemically Activated NiFeOxHyfor Enhanced Oxygen Evolution. *ACS Appl. Energy Mater.* **2021**, *4* (1), 595–

601. https://doi.org/10.1021/acsaem.0c02476.

(22) Song, F.; Zhang, T.; Zhou, D.; Sun, P.; Lu, Z.; Bian, H.; Dang, J.; Gao, H.; Qian, Y.; Li, W.; Jiang, N.; Dummer, H.; Shaw, J. G.; Chen, S.; Chen, G.; Sun, Y.; Rao, Y. Charge Transfer of Interfacial Catalysts for Hydrogen Energy. *ACS Mater. Lett.* **2022**, *4* (5), 967–977. https://doi.org/10.1021/acsmaterialslett.2c00143.

(23) Song, F.; Zhang, T.; Qian, Y.; Shaw, J.; Chen, S.; Chen, G.; Sun, Y.; Rao, Y. Multifunctional Electrocatalysts of Nickel Boride Nanoparticles for Superior Hydrogen Oxidation and Water Splitting. *Mater. Today Energy* **2021**, *22*, 100846. https://doi.org/10.1016/j.mtener.2021.100846.

(24) Ren, X.; Ge, R.; Zhang, Y.; Liu, D.; Wu, D.; Sun, X.; Du, B.; Wei, Q. Cobalt-Borate Nanowire Array as a High-Performance Catalyst for Oxygen Evolution Reaction in near-Neutral Media. *J. Mater. Chem. A* **2017**, *5* (16), 7291–7294. https://doi.org/10.1039/c7ta01027c.

(25) Tan, T.; Han, P.; Cong, H.; Cheng, G.; Luo, W. An Amorphous Cobalt Borate Nanosheet-Coated Cobalt Boride Hybrid for Highly Efficient Alkaline Water Oxidation Reaction. *ACS Sustain. Chem. Eng.* **2019**, *7* (6), 5620–5625. https://doi.org/10.1021/acssuschemeng.9b00258.

(26) Ge, R.; Du, H.; Tao, K.; Zhang, Q.; Chen, L. Cobalt-Borate Nanoarray: An Efficient and Durable Electrocatalyst for Water Oxidation under Benign Conditions. *ACS Appl. Mater. Interfaces* **2017**, *9* (18), 15383–15387. https://doi.org/10.1021/acsami.7b00184.

(27) Surendranath, Y.; Dincă, M.; Nocera, D. G. Electrolyte-Dependent Electrosynthesis and Activity of Cobalt-Based Water Oxidation Catalysts. *J. Am. Chem. Soc.* **2009**, *131* (7), 2615–2620. https://doi.org/10.1021/ja807769r.

(28) He, C.; Wu, X.; He, Z. Amorphous Nickel-Based Thin Film as a Janus Electrocatalyst for Water Splitting. *J. Phys. Chem. C* **2014**, *118* (9), 4578–4584. https://doi.org/10.1021/jp408153b.

(29) Bediako, D. K.; Surendranath, Y.; Nocera, D. G. Mechanistic Studies of the Oxygen Evolution Reaction Mediated by a Nickel-Borate Thin Film Electrocatalyst. *J. Am. Chem. Soc.* **2013**, *135* (9), 3662–3674. https://doi.org/10.1021/ja3126432.

(30) Chen, L.; Ren, X.; Teng, W.; Shi, P. Amorphous Nickel-Cobalt-Borate Nanosheet Arrays for Efficient and Durable Water Oxidation Electrocatalysis under Near-Neutral Conditions. *Chem. A Eur. J.* **2017**, *23*. https://doi.org/10.1002/chem.201702314.

(31) Suryawanshi, U. P.; Suryawanshi, M. P.; Ghorpade, U. V.; Shin, S. W.; Kim, J.; Kim, J. H. An Earth-Abundant, Amorphous Cobalt-Iron-Borate (Co-Fe-Bi) Prepared on Ni Foam as Highly Efficient and Durable Electrocatalysts for Oxygen Evolution. *Appl. Surf. Sci.* **2019**, *495* (March), 143462. https://doi.org/10.1016/j.apsusc.2019.07.204.

(32) Qian, Y.; Wu, Y.; Gu, F.; Zhou, Z.; Huang, Z.; Tang, X.; Pan, S.; Zhang, S.; Chen, S.; Zhang, Q.; Chen, Y.; Wang, S. Controllable and Scale-Up Synthesis of Nickel-Cobalt Boride@Borate/RGO Nanoflakes via Reactive Impingement Mixing: A High-Performance Supercapacitor Electrode and Electrocatalyst. *Front. Chem.* **2022**, *10*, 1–14. https://doi.org/10.3389/fchem.2022.874675.

(33) Ma, M.; Qu, F.; Ji, X.; Liu, D.; Hao, S.; Du, G.; Asiri, A. M.; Yao, Y.; Chen, L.; Sun, X. Bimetallic Nickel-Substituted Cobalt-Borate Nanowire Array An Earth-Abundant Water Oxidation Electrocatalyst with Superior Activity and Durability at Near Neutral PH. *Small* **2017**, *13* (1700394). https://doi.org/10.1002/smll.201700394.

(34) Jagiello, J.; Kenvin, J.; Celzard, A.; Fierro, V. Enhanced Resolution of Ultra Micropore Size

Determination of Biochars and Activated Carbons by Dual Gas Analysis Using N2 and CO2 with 2D- NLDFT Adsorption Models. *Carbon.* **2019**, *144*, 206–215. https://doi.org/10.1016/j.carbon.2018.12.028.

(35) Jagiello, J.; Kenvin, J.; Ania, C. O.; Parra, J. B.; Celzard, A.; Fierro, V. Exploiting the Adsorption of Simple Gases O2 and H2 with Minimal Quadrupole Moments for the Dual Gas Characterization of Nanoporous Carbons Using 2D-NLDFT Models. *Carbon.* **2020**, *160*, 164–175. https://doi.org/10.1016/j.carbon.2020.01.013.

(36) Bouleau, L.; Pérez-Rodríguez, S.; Quílez-Bermejo, J.; Izquierdo, M. T.; Xu, F.; Fierro, V.; Celzard, A. Best Practices for ORR Performance Evaluation of Metal-Free Porous Carbon Electrocatalysts. *Carbon.* **2022**, *189*, 349–361. https://doi.org/10.1016/j.carbon.2021.12.078.

(37) Filimonenkov, I. S.; Istomin, S. Y.; Antipov, E. V.; Tsirlina, G. A.; Savinova, E. R. Rotating Ring-Disk Electrode as a Quantitative Tool for the Investigation of the Oxygen Evolution Reaction. *Electrochim. Acta* **2018**, *286*, 304–312. https://doi.org/10.1016/j.electacta.2018.08.056.

(38) Fernandes, R.; Chunduri, A.; Gupta, S.; Kadrekar, R.; Arya, A.; Miotello, A.; Patel, N. Exploring the Hydrogen Evolution Capabilities of Earth-Abundant Ternary Metal Borides for Neutral and Alkaline Water-Splitting. *Electrochim. Acta* **2020**, *354*, 136738. https://doi.org/10.1016/j.electacta.2020.136738.

(39) Wang, P.; Chen, B.; Li, R.; Wang, S.; Ren, N.; Li, Y.; Mazumdar, S.; Shi, B.; Zhao, Y.; Zhang, X. Cobalt Chloride Hexahydrate Assisted in Reducing Energy Loss in Perovskite Solar Cells with Record Open-Circuit Voltage of 1.20 V. *ACS Energy Lett.* **2021**, 6, 2121–2128. https://doi.org/10.1021/acsenergylett.1c00443.

(40) Grosjean, R.; Le Godec, Y.; Delacroix, S.; Gouget, G.; Beaunier, P.; Ersen, O.; Ihiawakrim, D.; Kurakevych, O. O.; Chanéac, C.; Portehault, D. A High Pressure Pathway toward Boron-Based Nanostructured Solids. *Dalt. Trans.* **2018**, *47* (23), 7634–7639. https://doi.org/10.1039/c8dt00932e.

(41) Jung, H. J.; Nam, K.; Sung, H. G.; Hyun, H. S.; Sohn, Y.; Shin, W. G. Preparation of TiO2-Decorated Boron Particles by Wet Ball Milling and Their Photoelectrochemical Hydrogen and Oxygen Evolution Reactions. *Materials.* **2016**, *9* (12). https://doi.org/10.3390/ma9121012.

(42) Dutta, S.; Han, H.; Je, M.; Choi, H.; Kwon, J.; Park, K.; Indra, A.; Min, K.; Paik, U.; Song, T. Chemical and Structural Engineering of Transition Metal Boride towards Excellent and Sustainable Hydrogen Evolution Reaction. *Nano Energy* **2020**, *67*, 104245. https://doi.org/10.1016/j.nanoen.2019.104245.

(43) Liang, Y. C.; Wang, C. C. Surface Crystal Feature-Dependent Photoactivity of ZnO-ZnS Composite Rods: Via Hydrothermal Sulfidation. *RSC Adv.* **2018**, *8* (9), 5063–5070. https://doi.org/10.1039/c7ra13061a.

(44) Guo, M.; Gao, Y.; Shao, G. Complex Doping Chemistry Owing to Mn Incorporation in Nanocrystalline Anatase TiO2 Powders. *Phys. Chem. Chem. Phys.* **2015**, *18* (4), 2818–2829. https://doi.org/10.1039/c5cp05318h.

(45) Chia-ching, W.; Cheng-fu, Y. Investigation of the Properties of Nanostructured Li-Doped NiO Films Using the Modified Spray Pyrolysis Method. *Nanoscale Res. Lett.* **2013**, 8. https://doi.org/10.1186/1556-276X-8-33.

(46) Zhang, Q.; Zhao, J.; Wu, Y.; Li, J.; Jin, H.; Zhao, S.; Chai, L.; Wang, Y.; Lei, Y.; Wang, S. Rapid and Controllable Synthesis of Nanocrystallized Nickel-Cobalt Boride Electrode

Materials via a Mircoimpinging Stream Reaction for High Performance Supercapacitors. *Small* **2020**, *16* (39). https://doi.org/10.1002/smll.202003342.

(47) Mishra, A.; Sardar, M. Isolation of Genomic DNA by Silane-Modified Iron Oxide Nanoparticles. *Nanotechnol. Nov. Perspect. Prospect. McGraw Hill Educ. New York* **2015**, No. April, 309–315.

(48) Tugrul, N.; Acarali, N. B. Synthesis of Zinc Borate : Effects of Different Modifying Agents and Isopropyl Alcohol on Yield and Hydrophobicity by Using Zinc Carbonate. *Int. Conf. Chem. Chem. Process* **2011**, *10*, 55–58.

(49) Fazlali, F.; Mahjoub, A.; Abazari, R. A New Route for Synthesis of Spherical NiO Nanoparticles via Emulsion Nano-Reactors with Enhanced Photocatalytic Activity. *Solid State Sci.* **2015**, *48*, 263–269. https://doi.org/10.1016/j.solidstatesciences.2015.08.022.

(50) Liang, P.; Tuoheti, Z.; Liu, Z. H. Controlling the Structure and Morphology of Zinc Borate by Adjusting the Reaction Temperature and PH Value: Formation Mechanisms and Luminescent Properties. *RSC Adv.* **2017**, *7* (7), 3695–3703. https://doi.org/10.1039/C6RA23319H.

(51) Zamkovskaya, A.; Maksimova, E.; Nauhatsky, I. Orientation Dependence of the Thermal Expansion Coefficients of Iron Borate FeBo3 Crystals. *KnE Eng.* **2018**, *3* (4), 65. https://doi.org/10.18502/keg.v3i4.2226.

(52) Wu, C. Y.; Bao, Q.; Tsai, Y. T.; Duh, J. G. Tuning (003) Interplanar Space by Boric Acid Co-Sintering to Enhance Li+ Storage and Transfer in Li(Ni0.8Co0.1Mn0.1)O2 Cathode. *J. Alloys Compd.* **2021**, *865*, 158806. https://doi.org/10.1016/j.jallcom.2021.158806.

(53) Cui, L.; Zhang, W.; Zheng, R.; Liu, J. Electrocatalysts Based on Transition Metal Borides and Borates for the Oxygen Evolution Reaction. *Chem. - A Eur. J.* **2020**, *26* (51), 11661–

11672. https://doi.org/10.1002/chem.202000880.

(54) García-dalí, S.; Paredes, J. I.; Munuera, J. M.; Villar-rodil, S.; Martínez-alonso, A.; Tascón, J. M. D. An Aqueous Cathodic Delamination Route towards High Quality Graphene Flakes for Oil Sorption and Electrochemical Charge Storage Applications. *Chem. Eng. J.* **2019**, *372*, 1226–1239. https://doi.org/10.1016/j.cej.2019.04.201.

(55) Chen, P.; Xu, K.; Zhou, T.; Tong, Y.; Wu, J.; Cheng, H.; Lu, X.; Ding, H.; Wu, C.; Xie, Y. Strong-Coupled Cobalt Borate Nanosheets Graphene Hybrid as Electrocatalyst for Water Oxidation Under Both Alkaline and Neutral Conditions. *Angew. Chemie - Int. Ed.* **2016**, *55*, 2488–2492. https://doi.org/10.1002/anie.201511032.

(56) Hu, Q.; Li, G.; Han, Z.; Wang, Z.; Huang, X.; Chai, X.; Zhang, Q.; Liu, J.; He, C. General Synthesis of Ultrathin Metal Borate Nanomeshes Enabled by 3D Bark-Like N-Doped Carbon for Electrocatalysis. *Adv. Energy Mater.* **2019**, *9* (1901130). https://doi.org/10.1002/aenm.201901130.

(57) Ma, M.; Qu, F.; Ji, X.; Liu, D.; Hao, S.; Du, G.; Asiri, A. M.; Yao, Y.; Chen, L.; Sun, X. Bimetallic Nickel-Substituted Cobalt-Borate Nanowire Array: An Earth-Abundant Water Oxidation Electrocatalyst with Superior Activty and Durability at Near Neutral PH. *Small* **2017**,13, 1700394. https://doi.org/10.1002/smll.201700394.